Experimental Investigation of the $6s^2\,{}^1S_0 \rightarrow 5d6s\,{}^3D_{1,2}$ Forbidden Transitions in Atomic Ytterbium

(LBNL Preprint Number 42454)

C. J. Bowers†, D. Budker, S. J. Freedman,
G. Gwinner*, and J. E. Stalnaker
Lawrence Berkeley National Laboratory, Berkeley, California 94720
and Department of Physics, University of California, Berkeley, California 94720-7300

D. DeMille
Department of Physics, Yale University, New Haven, Connecticut 06520
(January 3, 1999)

We have observed the Stark-induced $6s^2\,{}^1S_0 \rightarrow 5d6s\,{}^3D_1$ transition in Yb and measured properties relevant to the study of atomic parity nonconservation in this transition. An atomic beam of Yb is excited by 408 nm light in the presence of an external DC electric field, resulting in cascade fluorescence at 556 nm as the excitation decays through the $6s6p\,{}^3P_1$ state. The density of the atomic beam and the fluorescence detection efficiency are calibrated by directly exciting the $6s6p\,{}^3P_1$ state with 556 nm light. Using an estimate of the ${}^3D_1 - {}^3P_1$ branching fraction, we obtain a measurement of the vector transition polarizability, $|\beta| = 2.18(33) \times 10^{-8}\ ea_0/(V/cm)$. In addition, we have observed the $6s^2\,{}^1S_0 \rightarrow 5d6s\,{}^3D_2$ transition at 404 nm. The electric quadrupole transition amplitude and tensor transition polarizability have been measured. We have also measured the DC Stark shifts, hyperfine structure, and isotope shifts for both transitions.

31.30.Gs, 32.10.Fn, 32.60.+i, 32.70.Cs

I. INTRODUCTION

The $6s^2\,{}^1S_0 \rightarrow 5d6s\,{}^3D_1$ transition in atomic ytterbium (Yb) has been identified as a promising system for precise measurements of parity nonconserving effects in atoms [1–3]. The parity nonconserving electric dipole transition amplitude ($E1_{\rm PNC}$) is estimated to be large relative to that of other heavy atoms that have been studied up to now (for reviews see e.g. [4–6]) and is measurable with the Stark-interference technique [7–10]. Comparison of $E1_{\rm PNC}$ measured in several of the seven stable isotopes of Yb may allow one to draw conclusions about electroweak parameters essentially independent of atomic structure calculations [11]. In addition, the nuclear anapole moments of ^{171}Yb (I=1/2) and ^{173}Yb (I=5/2) can be determined by comparing $E1_{\rm PNC}$ measured on different hyperfine components. Each of these Yb nuclei has a valence neutron, while ^{133}Cs has a valence proton. Thus, anapole moment measurements in Yb would complement the recent measurement of the ^{133}Cs anapole moment [10] in the determination of weak meson-nucleon coupling parameters.

In the absence of an external electric field, the $6s^2\,{}^1S_0 \rightarrow 5d6s\,{}^3D_1$ transition at 408 nm (Figure 1) is highly suppressed. Angular momentum selection rules allow only dipole transitions. However, the electric dipole transition amplitude between two states of the same nominal parity is due only to parity mixing by the weak interaction. The most precise estimate of the size of this effect gives $E1_{\rm PNC} = -i\,1.09(25) \times 10^{-9}$ ea$_0$ [2]. The magnetic dipole ($M1$) amplitude is highly suppressed due to configuration and L-S coupling selection rules. Configuration interaction and spin-orbit interaction are expected to contribute only in a high order of perturbation theory, leading to an M1 amplitude of $M1 \lesssim 10^{-4}\ \mu_B$ [1]. In the present work, we set a crude limit $|M1| < 1.5 \times 10^{-2}\ \mu_B$, and a more sensitive Stark-interference measurement of $M1$ is underway.

An $E1$ transition amplitude can be induced by applying an external DC electric field, which mixes states of opposite parity. With an applied electric field of 45 kV/cm, the Stark-induced amplitude is $E1_{St} \approx 10^{-3}$ ea$_0$. In the measurements presented here, we observe the transition rate due to $|E1_{St}|^2$. We have measured the absolute strength of $E1_{St}$, which is parameterized by the vector transition polarizability, β. We have also measured frequency shifts associated with the 408 nm transition: Stark shifts, isotope shifts, and hyperfine structure.

The $6s^2\,{}^1S_0 \rightarrow 5d6s\,{}^3D_2$ transition at 404 nm may also be of interest for PNC measurements. For this transition only the nuclear spin-dependent weak Hamiltonian contributes to $E1_{\rm PNC}$. We have measured the Stark shifts, isotope shifts and hyperfine structure of the 404 nm transition, as well as the absolute strength of the $E2$ and Stark-induced amplitudes — the latter parameterized by the tensor transition polarizability, γ.

II. EXPERIMENTAL APPARATUS

Since essentially the same apparatus was used for both the 404 and 408 nm transitions, we limit the discussion to measurements on the 408 nm transition, discussing the 404 nm measurements only when the two differ. CW violet light is generated by frequency-doubling the IR out-

put of a Ti:sapphire laser in an external cavity doubler. The 408 nm light interacts with a mechanically chopped atomic beam passing between two electric field plates (Figure 2). Excitation of the $6s^2\,{}^1S_0 \rightarrow 5d6s\,{}^3D_1$ state is detected by observing fluorescence at 556 nm from decay through $6s6p\,{}^3P_1$ to the ground state (Figure 1). The 556 nm fluorescence is detected with a photomultiplier tube.

For the measurement of the absolute strength of the Stark-induced amplitude a second CW laser beam, at 556 nm, was used to excite the $6s^2\,{}^1S_0 \rightarrow 6s6p\,{}^3P_1$ transition directly. The ratio of signals due to excitation by the two wavelengths is independent of detection efficiency and atomic beam column density; it depends only on the ratio of transition probabilities, angular coefficients, and light powers. Since the absolute strength of this transition is known from the $^3P_1$ lifetime, the $6s^2\,{}^1S_0 \rightarrow 5d6s\,{}^3D_1$ transition amplitude can be determined also.

A. Light Sources at 408 and 556 nm

Light at 816 nm is generated with a cw Ti:sapphire laser (Schwarz Electro-optics Titan-CW) pumped with all lines of an Ar^+ laser (Spectra-Physics 2080). The Ti:sapphire laser was modified to give single mode output, continuously scanable over ≈20 GHz. The basic plan for these modifications was adapted from Ref. [12] and details can be found in Ref. [13]. The effective length of the laser cavity is controlled by dual tilt plates and by a mirror mounted on a piezoelectric element (PZT). Single mode lasing is ensured with a 3 mm uncoated quartz intra-cavity etalon; a transmission peak of the etalon is made to track the laser frequency. To accomplish this, the angle of the etalon is dithered, and the reflection from it is minimized with a feedback circuit.

The frequency of the 816 nm light is locked to a transmission peak of a temperature-stabilized scanable confocal Fabry-Perot (FP) etalon with a 150 MHz free spectral range (Burleigh CFT-500). The Pound-Drever-Hall FM sideband locking technique [14] is used. When locked, the laser linewidth is ≈0.5 MHz while the long-term drift is about 10 MHz/hr. The frequency of the 816 nm light is scanned by changing the length of the FP.

The $^3D_1$ transition requires light at 408.344 nm (vacuum), which we get by frequency doubling of light at 816.689 nm. Unfortunately, there is a strong water vapor absorption line at 816.678 nm [15,16] which creates a tuning gap of ≈0.04 nm for the Ti:sapphire laser, suppressing lasing at the desired wavelength. Sealing the laser cavity and purging it with dry nitrogen reduces the effect of the water vapor, but it is also necessary to use an additional 0.1 mm coated etalon in the laser cavity to achieve a continuous frequency scan across the region of interest.

The 816 nm light is coupled into an external cavity frequency doubler (Laser Analytical Systems Wavetrain-CW) using lithium triborate (LBO) as the non-linear crystal. For 1.5 W at 816 nm, we get 250 mW at 408 nm.

Light at 556 nm, exciting the $^1S_0 \rightarrow {}^3P_1$ transition, was obtained with a ring dye laser (Spectra-Physics 380D) pumped with a portion of the light from the same Ar^+ laser used to pump the Ti:sapphire laser. The laser dye is Rhodamine 110, and the frequency is stabilized using a dual Fabry-Perot system (Spectra-Physics 388/389) resulting in a linewidth of ≈1 MHz.

B. Atomic Beam and Interaction Region

The Yb atomic beam propagates inside a vacuum chamber and is generated by a stainless steel oven 15 cm long and 5 cm in diameter. (Yb was found not to react with 304 stainless steel up to at least 570° C.) Atoms leave the oven through a series of vertical channels 0.5 cm deep which were cut using a wire electric discharge machine with 0.025 cm wire. The 32 channels cover an area 0.5 cm high by 1.9 cm wide with a transparency of ≈50%.

The oven is resistively heated with thermocoax heating elements clamped to its exterior. To avoid clogging of the oven channels, the front of the oven is kept ≈30° C hotter than the rear. Radiative cooling is reduced with three layers of heat shielding. The rear of the oven is typically operated at 500° C.

In order to implement a lock-in detection technique, the atomic beam is mechanically chopped at ≈310 Hz with an in-vacuum chopper wheel. The phase of the atomic beam modulation is monitored with an LED/photodiode pair.

Electric field plates are located 11 cm from the front of the oven and are separated by 1.016 cm vertically. The atomic beam is collimated in the vertical dimension to reduce the amount of Yb deposited on the field plates. Horizontal collimation is accomplished by the oven channels, resulting in an observed Doppler width of 110 MHz in the 408 nm transition. From absorption measurements on the 556 nm transition, the density of Yb atoms in the interaction region is estimated to be $2 \times 10^{10}/\mathrm{cm}^3$. This is in reasonable agreement with the value expected from the saturated vapor pressure and geometrical considerations in the effusive regime.

The laboratory magnetic field of a few hundred milligauss in the interaction region was reduced to ≈15 mG using 3 pairs of current coils on the exterior of the vacuum chamber. The coils around the vertical axis (z-direction) were also used to create a 1.3 G bias field. This field was applied in order to simplify the angular distribution of fluorescence due to excitation of the 404, 408, and 556 nm transitions in the presence of DC electric fields. This is discussed in Appendix A.

C. Fluorescence Detection

The top electric field plate has an array of 198 holes, each with 0.12 cm diameter, allowing fluorescence from the atomic beam to be collected by a Lucite light guide and conducted to a photomultiplier tube (Burle 8850). The thickness of the electrode at the location of the hole array was 0.12 cm, providing for ≈50% transmission for the angles within the field of view (see below). The presence of the holes in the top field plate reduces the electric field between the plates. This effect was calculated to be less than 1% using a random walk solution to Laplace's equation [17].

Light conducted along the light guide passed through an interference filter centered at 560 nm with a 10 nm FWHM. The light guide was enclosed in an aluminum tube to prevent the entrance of light not originating from the interaction region. It was observed that even small amounts of 408 nm light scattered by the vacuum chamber windows into the Lucite light guide produced fluorescence near 560 nm and resulted in a large background in the phototube signal. This problem was reduced by gluing a piece of GG10 Schott color glass to the front of the light guide to attenuate the 408 nm light before it could produce fluorescence in the light guide.

The phototube current was averaged in an integrator which was gated with logic signals from the chopper wheel corresponding to the atomic beam being open and closed. The output of the gated integrator was digitized, and the values corresponding to the atomic beam being open and closed were subtracted. For each point in a laser frequency scan, signals from 100-1000 atomic beam chop cycles were averaged.

III. SPECTROSCOPY OF THE 408 NM TRANSITION

The laser-excitation spectrum for the 408 nm transition is shown in Figure 3. There is significant overlap between several of the even isotopes and hyperfine components of the odd isotopes. Based on measurements of hyperfine structure and isotope shifts described below, as well as the known isotopic abundances, the expected contributions to the isotope and hyperfine components have been separated in the lower half of Figure 3. For the least abundant isotope, ^{168}Yb, which has a natural abundance of only 0.135%, the signal is expected to be within 10 MHz of the $F = 1/2 \rightarrow F' = 1/2$ component of ^{171}Yb, which is ≈ 50 times stronger.

These measurements were made with ≈10 mW of laser power at 408 nm, observing in the 556 nm fluorescence channel. A static electric field up to 45 kV/cm was applied. The polarization of the excitation light was linear, at 90° to the electric field direction.

Measurement of isotope shifts, hyperfine structure, and DC Stark shifts all require measurement of differences in optical transition frequencies. The drift and jitter of the FP to which the Ti:sapphire laser was locked was the limiting factor in the frequency determination. We observed drifts of ≈20 MHz/hour in the 408 nm transition and scan-to-scan frequency jitter of ≈4 MHz. Non-linearity in the FP frequency as a function of applied voltage was measured by locking the laser to adjacent FP transmission peaks as they scanned across a single component of the atomic resonance. Voltages corresponding to the peak of the atomic resonance were fit with a third-order polynomial to calibrate the frequency-to-voltage relation of the PZT-controlled FP.

The line center of each fluorescence peak was determined with a least-squares fit. The shape of each peak is dominated by the Doppler broadening associated with the transverse velocity distribution of the atomic beam. The distribution is not a Gaussian, due to the collimation of the thermal source. For peaks which are sufficiently isolated, the line center was determined by fitting a Lorentzian, with variable line center, line width, and amplitude, in a range one FWHM around the peak. This simple line-shape model was adequate for determining isolated peak positions.

For peaks which overlap one another, both peaks were fit simultaneously with a more complex function that better matches the tails of the distribution. The line-shape function was determined by looking at isolated peaks from the same data set. It was found empirically that the line shape of an isolated peak is well described by the sum of a Gaussian and a Lorentzian with the same line center, different widths, and different amplitudes. The widths and relative amplitudes of the Gaussian and Lorentzian for the single-peak curve were fixed by the fit to an isolated peak. Overlapping peaks were then fit with the sum of two single-peak curves with variable line centers and overall amplitude. The relative amplitudes of the two single-peak curves were fixed by the relative isotopic abundances and angular momentum considerations.

A. Stark Shifts

DC Stark shifts were measured with electric fields ranging from 15 to 45 kV/cm. The maximum shift observed amounted to only 20 MHz. In order to minimize the effect of the drift of the FP, Stark shifts were measured by taking a series of short frequency scans over a single peak (scanning ≈3 FWHM of the peak), alternating the electric field strength between 45 kV/cm and a lower value from one scan to the next.

All of the Stark shifts for the sublevels of a given energy level depend on at most two atomic parameters, $\alpha_0(\gamma J)$ and $\alpha_2(\gamma J)$, the scalar and tensor polarizabilities. As shown in Ref. [18], in the absence of the hyperfine interaction, the Stark shift for a magnetic sublevel, $|\gamma, Jm_J\rangle$, is

$$\varepsilon(\gamma J m_J) = -\frac{1}{2}\Big(\alpha_0(\gamma J) + \alpha_2(\gamma J)\frac{3m_J^2 - J(J+1)}{J(2J-1)}\Big)E^2, \quad (3.1)$$

where E is the electric field. For $J = 0$ and $J = 1/2$, the tensor polarizability α_2 is identically zero.

Including the hyperfine interaction, the Stark shift of a magnetic hyperfine sublevel, $|\gamma J, F m_F\rangle$, is

$$\varepsilon(\gamma JI, F m_F) = -\frac{1}{2}\Big(\alpha_0(\gamma JIF) + \alpha_2(\gamma JIF)\frac{3m_F^2 - F(F+1)}{F(2F-1)}\Big)E^2. \quad (3.2)$$

Again, for $F = 0$ and $F = 1/2$, only the scalar polarizability contributes to the shift. In general, $\alpha_0(\gamma JIF) = \alpha_0(\gamma J)$. However, the relation between $\alpha_2(\gamma JIF)$ and $\alpha_2(\gamma J)$ is more complicated and is given in Ref. [18].

We measured the Stark shifts of the ^{174}Yb peak and the $F = 1/2 \rightarrow F' = 1/2$ component of ^{171}Yb. Since only the vector transition polarizability contributes to this Stark-induced transition, with a static electric field in the z-direction, we can excite only $\Delta m = \pm 1$ transitions among sublevels (See Eq. 5.2). For the even isotopes we thus excite only the $m_J = \pm 1$ states.

We use the $F = 1/2 \rightarrow F' = 1/2$ component of ^{171}Yb because only the scalar polarizability contributes to the shift. For each transition, approximately 50 frequency scans were taken. We find:

$$\Delta\nu(171, F = 1/2 \rightarrow F' = 1/2) = 10.8(4)\ E^2 \frac{\text{kHz}}{(\text{kV/cm})^2}$$
$$\Delta\nu(174, m_J = \pm 1) = 7.3(3)\ E^2 \frac{\text{kHz}}{(\text{kV/cm})^2}. \quad (3.3)$$

Using Eqs. 3.1 and 3.2 to relate the Stark shift rates to the scalar and tensor polarizabilities, we solve for the polarizabilities, yielding

$$\alpha_0(^3D_1) - \alpha_0(^1S_0) = -21.6(8)\ \frac{\text{kHz}}{(\text{kV/cm})^2}$$
$$\alpha_2(^3D_1) = 7.0(10)\ \frac{\text{kHz}}{(\text{kV/cm})^2}. \quad (3.4)$$

We can unambiguously determine the tensor polarizability for the $^3D_1$ state. However, the relative contributions of $\alpha_0(^3D_1)$ and $\alpha_0(^1S_0)$ cannot be distinguished in this measurement.

B. Hyperfine Structure and Isotope Shifts

The results obtained for the peak positions of even isotopes and the hyperfine components of odd isotopes are given in Table I. The shifts are given relative to ^{174}Yb since it is the strongest component and is sufficiently isolated. These results were obtained by averaging the shifts from about 6 scans involving any given peak. The largest rms deviation of any set of shifts was about 5 MHz, so an error of 2 MHz was assigned to each average. This uncertainty is consistent with the drift and jitter of the FP.

These frequency shift measurements were made using a 45 kV/cm electric field to generate a Stark-induced amplitude. Therefore, each level also experiences a Stark shift. For the even isotopes, we only excite the $m_J = \pm 1$ magnetic sublevels, as discussed above. These sublevels are Stark shifted by the same amount, so the frequency differences among even isotopes are unaffected by the electric field. However, the magnetic hyperfine sublevels excited in the odd isotopes have different Stark shifts. It is shown in Ref. [13], that in order to determine the hyperfine constants it is necessary to apply small corrections ($\approx$7 MHz at an electric field of 45 kV/cm) to the measured peak positions. The results given in Table II include these corrections.

Previous measurements of A and B for the $^3D_1$ state [19] were made using a hollow cathode lamp by exciting the $^3D_1$ state to several higher lying states with a Ti:sapphire laser. The results of the present work are in agreement with those of Ref. [19]. The constants A and B were also calculated by Ref. [20] and are within a few percent of the experimental values.

The isotope shift of an atomic transition frequency is the sum of the field shift (FS), normal mass shift (NMS), and specific mass shift (SMS) [21]. The FS is due to the change in the spatial distribution of the nuclear charge between isotopes. The NMS is due to the change in the reduced mass of the electron-nucleus system and is readily calculated. The SMS is due to momentum correlations among electrons and is more difficult to calculate. The presence of the SMS prevents the direct extraction of the FS from measured isotope shifts. As pointed out by King [22], by plotting isotope shifts for two different transitions against one another, one can extract the ratio of field shifts for the two transitions and relate the specific mass shifts. The isotope shifts measured in the $6s^2\,^1S_0 \rightarrow 6s6p\,^3P_1$ transition [23] along with the present measurements have been used to perform a King plot analysis. The data are fit well with a line yielding the following two relations (in MHz):

$$\text{FS}_{408} = 1.136(9) \times \text{FS}_{556}$$
$$\text{SMS}_{408} = 1.136(9) \times \text{SMS}_{556} + 20(10). \quad (3.5)$$

The observed ratio of the field shifts is consistent with the assumption that the three levels involved, $6s^2\,^1S_0$, $6s6p\,^3P_1$ and $5d6s\,^3D_1$, are pure configurations [13] and is in agreement with the calculations of Refs. [24,25]. The relatively small difference in specific mass shifts for the two transitions is also consistent with both specific mass shifts being small, as one would expect if no f electrons are excited [21].

IV. SPECTROSCOPY OF THE 404 NM TRANSITION

Here we present Stark shift, isotope shift, and hyperfine structure measurements for the 404 nm transition. We will only describe those details that differ significantly from the description in the previous section.

The fluorescence signal as a function of frequency for the 404 nm transition is shown in the upper part of Figure 4. The various isotopic and hyperfine components are identified in the lower part.

A. Stark Shifts

The ^{172}Yb isotope was used for the measurement of the Stark shifts of the $^3D_2$ transition since, in this case, it is the strongest isolated component. The measurement is complicated by the fact that magnetic sublevels with different values of $|m_J|$ are excited in proportions that vary as a function of electric field. This is due to the fact that the transition is excited by a combination of electric quadrupole and Stark-induced electric dipole transition amplitudes, as discussed in Section VI. Since different m_J sublevels have different Stark shifts, the Stark shift of the signal will depend on the relative contribution of each m_J sublevel to that signal.

In Section VI, we derive the relative contribution of each m_J sublevel to the fluorescence signal for a given polarization of excitation light. Combining that with the measured strengths of the E2 and Stark-induced amplitudes presented there, we can model the shift of the fluorescence signal as a function of applied electric field, using only two free parameters: $(\alpha_0(^3D_2) - \alpha_0(^1S_0))$ and $\alpha_2(^3D_2)$. (See Ref. [13] for details.)

Using Stark shift measurements for z and y polarized excitation light and fitting for the two free parameters, we find

$$\alpha_0(^3D_2) - \alpha_0(^1S_0) = -20(1)\ \frac{\text{kHz}}{(\text{kV/cm})^2}$$
$$\alpha_2(^3D_2) = 7(2)\ \frac{\text{kHz}}{(\text{kV/cm})^2}. \qquad (4.1)$$

B. Hyperfine Structure and Isotope Shifts

The results obtained for the peak positions of even isotopes and the hyperfine components of odd isotopes are given in Table III. The peak positions are measured relative to the ^{172}Yb peak for reasons stated above. For overlapping peaks the uncertainties are larger than for relatively isolated peaks.

Since the frequency shifts were measured with a nonzero electric field applied, the hyperfine components of odd isotopes need to be corrected for their different Stark shifts. These corrections ($\lesssim$ 4 MHz at 33kV/cm) are taken into account in Table IV, which gives the center of gravity and hyperfine constants for ^{171}Yb and ^{173}Yb. Our measurements of A and B for $^3D_2$ have similar uncertainties compared to Ref. [19] and the two measurements are in good agreement. Again, A and B were calculated by Ref. [20] and are within a few percent of the experimental values.

The isotope shifts for the 404 nm transition are nearly identical to those in the 408 nm transition given in the previous section. A King plot analysis for the two transitions yields the following two relations (in MHz):

$$\text{FS}_{404} = 0.98(1) \times \text{FS}_{408}$$
$$\text{SMS}_{404} = 0.98(1) \times \text{SMS}_{408} + 20(15) \qquad (4.2)$$

The field shifts and specific mass shifts for the two transitions are nearly equal. Again, this is consistent with pure configuration assignments for the two levels [24,25].

V. VECTOR TRANSITION POLARIZABILITY OF THE 408 NM TRANSITION

Here we describe an absolute measurement of the vector transition polarizability, β, for the $6s^2\,{}^1S_0 \rightarrow 5d6s\,{}^3D_1$ transition. We measure the fluorescence at 556 nm due to excitation of the $5d6s\,{}^3D_1$ state and decay through the $6s6p\,{}^3P_1$ state for a specific power of 408 nm light incident on the atomic beam in a specific electric field. We measure the fluorescence at 556 nm due to direct excitation of the $6s6p\,{}^3P_1$ state for a specific power of 556 nm light incident on the atomic beam. The ratio of the fluorescence signal induced by 408 nm light, normalized to the light power at 408 nm, and the corresponding quantity for the 556 nm excitation is independent of detection efficiency and atomic beam column density. Using this method to determine $|\beta|$ requires knowledge of the strength of the 556 nm calibration transition and also of the $^3D_1 - {}^3P_1$ branching fraction.

A. Estimates of β

In the presence of a static electric field, $\mathbf{E}$, and an oscillating electric field, $\boldsymbol{\varepsilon}$, due to the laser light, the Stark-induced amplitude between the perturbed $|{}^1S_0, 0\rangle$ state and the perturbed $|{}^3D_1, m\rangle$ state is [26]

$$E1_{St} = \langle \overline{5d6s\,{}^3D_1, m}| -\mathbf{d}\cdot\boldsymbol{\varepsilon}\,|\overline{6s^2\,{}^1S_0, 0}\rangle$$
$$\equiv i\beta(\mathbf{E}\times\boldsymbol{\varepsilon})_m. \qquad (5.1)$$

$|\overline{\ \ }\rangle$ denotes the state perturbed by the static electric field and $(\mathbf{E}\times\boldsymbol{\varepsilon})_m$ is a component of an irreducible spherical tensor. β, the vector transition polarizability, completely determines the strength of this Stark-induced

transition for any arrangement of $\mathbf{E}$ and ε. Only the vector transition polarizability contributes since the transition is $J = 0 \rightarrow J' = 1$. Written in terms of Cartesian components, we have

$$\begin{aligned} E1_{St} = & i\beta(\mathbf{E}\times\varepsilon)_z\delta_{m,0} \\ & -\frac{i\beta}{\sqrt{2}}((\mathbf{E}\times\varepsilon)_x + i(\mathbf{E}\times\varepsilon)_y)\delta_{m,+1} \\ & +\frac{i\beta}{\sqrt{2}}((\mathbf{E}\times\varepsilon)_x - i(\mathbf{E}\times\varepsilon)_y)\delta_{m,-1}. \end{aligned} \tag{5.2}$$

Due to the small energy separation between the $^3D_1$ and $^1P_1$ levels, the strength of the $^1S_0$ to $^1P_1$ transition, and significant singlet-triplet mixing, the dominant contribution to β comes from the Stark mixing of $^1P_1$ into $^3D_1$. Considering only this dominant contribution,

$$\beta \approx -\frac{e^2}{3\sqrt{2}}\frac{(^3D_1\|r\|^1P_1)(^1P_1\|r\|^1S_0)}{E(^3D_1) - E(^1P_1)}. \tag{5.3}$$

The reduced matrix element $(^1P_1\|r\|^1S_0)$ can be readily determined from the lifetime of the $^1P_1$ level, while $(^3D_1\|r\|^1P_1)$ can be determined from the $^3D_1$ lifetime, certain assumptions about the $^3D_1$ branching fractions, and the ($^3P_1$ -$^1P_1$) spin-orbit mixing coefficients. A complete discussion of the experimental data used in determining the reduced matrix elements can be found in Ref. [13]. Using those values for the matrix elements, we estimate that

$$\begin{aligned} |\beta| &= 110(20)\ \mathrm{a_0}^3 \\ &= 2.1(4)\times 10^{-8}\ \mathrm{ea_0/(V/cm)} \quad \text{(estimate)}. \end{aligned} \tag{5.4}$$

We have given the result in both natural and more practical units to facilitate comparison with other estimates. This estimate is different from that given in Ref. [1] by a factor of 2.5, even though the inputs are essentially the same. This is due to a numerical error in Ref. [1].

A value for β has also been calculated in an *ab initio* calculation [2] yielding

$$\beta = -138(30)\ \mathrm{a_0}^3 \quad \text{(estimate)}. \tag{5.5}$$

B. Experimental Technique

In order to control the intensity of the 408 and 556 nm beams, the light was passed through color glass and crossed linear polarizers. The power must be reduced during the measurement to avoid saturation of the transition, as discussed below. The polarizations of both the 408 nm beam and the 556 nm beam were controlled with independent $\lambda/2$ plates.

The 556 nm beam was combined with the 408 nm beam with a dichroic mirror. Both beams were expanded to ≈6 mm diameter and then apertured by a 2 mm iris diaphragm. In order to reduce sensitivity to spatial inhomogeneity in the atomic beam, the two laser beams were focused with an f=50 cm lens located immediately after the iris diaphragm. The two beams were made collinear by aligning the beam spots immediately before and far after the chamber.

It is important that the comparison of the transition rates for the two transitions is not affected by saturation effects. The calculated diameters of the two focused laser beams were 0.13 and 0.18 mm, respectively. Even though there are metastable states in the decay channels of $^3D_1$, the ground state population in the interaction region is replenished by the motion of atoms in the atomic beam. Since the transit time across the laser beam is on the order of the natural lifetime, one must take into account transit broadening of the laser light in order to properly calculate the transition probability for an atom crossing the laser beam. This was done by numerically integrating the optical Bloch equations for an atom traversing a Gaussian laser beam [27]. These calculations show that the depletion of the ground state by optical pumping can be kept to less than 1% by using optical power less than 700 μW for 408 nm light with a 50 kV/cm electric field. At lower electric fields, this limit is raised in inverse proportion to the square of the electric field. For 556 nm light, depletion of the ground state was kept below 1% by making measurements with less than 6.5 nW of incident power.

The light transmitted through the chamber was separated into 408 nm and 556 nm components with another dichroic mirror. Each beam was focused onto a silicon photodiode. It was necessary to lower the incident power of the 408 nm beam to less than 100 μW in order to avoid saturation effects in the photodiode. The linearity of the photodiodes below this power was tested by comparing the signal from the photodiode under test with a second photodiode sampling 10 times less power, over a range of incident powers. The photodiode currents were synchronously integrated, referenced to the atomic beam chopper and digitized along with the integrated phototube current, as described in Section II.

For the 556 nm transition, the ^{172}Yb, ^{174}Yb, and ^{176}Yb components were used. The different components of the 556 nm transition were identified using Ref. [23]. For the 408 nm transition, only the ^{174}Yb component was used, since it is the largest even isotope that has no significant overlap with a hyperfine component, as shown in Figure 3. The contribution of $F = 5/2 \rightarrow F' = 5/2$ of ^{173}Yb to the ^{174}Yb signal at line center is 0.5% at moderate oven temperatures. At higher oven temperatures, the Doppler width of the atomic beam increases, due to self-scattering of the atomic beam. This leads to a larger overlap between the two components. However, even at the highest oven temperature used, the contribution was only 1.5%. A corresponding correction was included for data taken at high oven temperatures.

Measurements of the relative fluorescence signals were made by alternating between 408 and 556 nm frequency scans with one of the two laser beams blocked. Each frequency scan spanned ≈1 GHz (≈500 frequency points,

50 atomic beam chop cycles per frequency point) across the line center of the component. The fluorescence signals differ by about one order of magnitude at the incident powers used.

C. Calibration and Systematics

The angular distribution of 556 nm fluorescence from the $^3P_1$ level depends on how it is populated. Direct excitation of $^3P_1$ with 556 nm light produces fluorescence with an angular distribution different from that produced by excitation of $^3D_1$ with 408 nm light and the subsequent decay through $^3P_1$ to the ground state. In order to accurately determine the relative strengths of the two transitions, one must take into account the different angular distributions.

A detailed calculation of the angular distributions for fluorescence from the even isotopes is described in Appendix A. This derivation, combined with measurements of the fluorescence signal after 556 nm excitation with z-polarization relative to y-polarization, yields

$$\frac{\frac{F(408,\hat{y})}{I(408,\hat{y})}}{\frac{1.15}{2}\frac{F(556,\hat{y})}{I(556,\hat{y})}} = \frac{\beta^2 E^2 BF_1}{\frac{1}{3}e^2|(^3P_1\|r\|^1S_0)|^2}\ \frac{408.3}{555.8}. \qquad (5.6)$$

Here $F(408,\hat{y})$, for example, refers to the fluorescence signal (always at 556 nm) due to y-polarized 408 nm light with power $I(408,\hat{y})$. The reduced matrix element is determined from the $^3P_1$ lifetime. BF_1 is the $^3D_1 \rightarrow ^3P_1$ branching fraction, and the factor 408/556 accounts for the different Doppler widths of the two transitions. When making measurements using different isotopic components for the two transitions, this formula is modified to take into account the natural isotopic abundances.

The photodiodes were calibrated using two optical power meters with calibrated optical heads (Newport Model 818-UV). Despite the accuracy of ±2% relative to the NIST standard specified for this model of power meter, our measured differences for the readings for the two power meters were 2% and 4% at 408 and 556 nm, respectively. Calibrations performed over the course of several months also differed by a few percent. We take the average of several calibrations for each photodiode and assign an uncertainty of ±4% to the absolute calibration. The power was also corrected for the measured transmission of the vacuum chamber windows. The absorption of 556 nm light (typically a few percent) by the atomic beam reduces the measured power relative to the power averaged over the atomic beam, so the absorption of the 556 nm beam was monitored and used to correct for this effect.

Nonuniformity of the fluorescence detection efficiency along with transverse displacements of the laser beams relative to their direction of propagation can lead to errors in the determination of the relative transition probabilities. In the worst case, 408 and 556 nm beams are separated by 1 mm in any direction. Geometrical considerations show that this results in at most a 1% difference in detection efficiencies. We also checked for this effect by deliberate misalignment of the laser beams.

With a dense atomic beam, radiation trapping can also affect fluorescence signals. However, this alters the 556 nm fluorescence distribution in similar ways for the 408 and 556 nm excitation transitions, and should have no significant effect on the measurement of $|\beta|$. Nevertheless, this was checked for by comparing data taken on isotopes with different abundances (and therefore different densities) and data taken at different overall atomic beam densities.

As noted in Ref. [28], for an absolute measurement of this kind it is important to understand the spectral profile of the lasers being used. Although we assume that the laser linewidth is much smaller than the Doppler linewidth, there may be a broad frequency component in addition to the primary longitudinal mode of the laser. This broad pedestal would contribute to the measured total power of the laser beam, but not to the fluorescence signal. Auxiliary measurements of both 408 and 556 nm laser spectra indicate that any broad spectral component is much less than 1% of the total power.

D. Analysis and Results

The ratio of fluorescence signal to incident power, F/I in Eq. 5.6, is calculated for each frequency point in a scan. We determine the value of F/I on line center by fitting this curve to a single Lorentzian, using 15 points (spread over ≈30 MHz) on either side of line center.

The uncertainty in the signal size for a single frequency point is typically ≈5% of the on-resonance signal size for the 408 nm transition and ≈1% for the 556 nm transition. The noise was determined from the rms deviation calculated for each set of 50 beam chop cycles and is roughly consistent with shot noise in the phototube, with phototube currents of ≈2 nA and 20 nA for the 408 nm and 556 nm transitions, respectively. Since the value of F/I on line center is fit using 30 points, the statistical uncertainty in that value is reduced to about 1% for the 408 nm transition.

Since frequency scans alternated between the two transitions about once a minute, fluctuations of the atomic beam density, PMT gain, and photodiode circuit gain, as well as occasional electrical discharges, can result in additional variation in the value of $|\beta|$ extracted from alternating scans. The rms deviation of the fitted peak intensity for successive scans on the same transition was measured to be ≈2% of the signal size.

In the data analysis, one to five consecutive frequency scans on each transition were grouped into sets. Each scan in a set was taken under nominally identical conditions. Using the measured ratio of $\frac{F(556,\hat{z})}{I(556,\hat{z})}/\frac{F(556,\hat{y})}{I(556,\hat{y})}$, the mean of $F(408,\hat{y})/I(408,\hat{y})$ and $F(556,\hat{y})/I(556,\hat{y})$

in each set was used to calculate a value of $|\beta|$ using Eq. 5.6.

Figure 6 shows the values of $|\beta|$ determined from 16 sets of frequency scans, comprising a total of ≈100 scans taken on 3 different days. The error bars in Figure 6 represent the uncertainties in the mean for each set determined from the rms deviation of $F(408,\hat{y})/I(408,\hat{y})$ and $F(556,\hat{y})/I(556,\hat{y})$ for the scans in the set.

Using the mean values and uncertainties for each set, we find the weighted mean of $|\beta|$ for all 16 sets to be 2.18×10^{-8} ea$_0$/(V/cm). However, the reduced χ^2 is 2.0 indicating additional variation over longer time scales. The rms deviation of $|\beta|$ for the 16 data sets is 1.5%. Taking a conservative approach, we use this rms deviation as the error in the weighted mean (without dividing by $\sqrt{15}$.) This variation is not the dominant source of uncertainty, so it does not significantly increase the overall uncertainty.

For these data sets, we intentionally varied experimental parameters not expected to change the result. The measurements of $|\beta|$ were made using electric fields ranging from 20 to 40 kV/cm. The density of the atomic beam was varied by a factor of 10 over these measurements by adjusting the oven temperature. The gain of the photomultiplier tube was varied by a factor of 10. In addition, the strength of the magnetic field in the z-direction was increased from 1.3 to 2 G. (See Appendix A for discussion of the effects of the magnetic field.) For Run B the physical width of the atomic beam was narrowed from the 2 cm used in Runs A and C down to 1 cm using collimators. No systematic variation in the measured value of $|\beta|$ was observed as a result of any of these changes.

In order to test our assumptions about the sizes of known systematic errors and to look for unforeseen sources of error, data was also taken while making larger changes to the experimental parameters. These changes were large enough that one might expect them to disturb the accuracy of the measurement, so they were not included in the final weighted mean. In order to test the sensitivity of the measurement to relative alignment of the 408 and 556 nm beams, the 408 nm beam was intentionally misaligned by ≈1 mm in the horizontal direction and again in the vertical direction. As another test, the lens which focuses both 408 and 556 nm beams into the interaction region was removed. These changes resulted in deviations of at most 5% in the measured values of $|\beta|$.

Determining $|\beta|$ from the measurement of fluorescence at 556 nm due to excitation of the 408 and 556 nm transitions requires knowledge of both the reduced matrix element, $(^3P_1\|r\|^1S_0)$, and the $^3D_1$ - $^3P_1$ branching fraction. We use $|(^3P_1\|r\|^1S_0)| = 0.549(4)\ a_0$ [13] and $BF_1(^3D_1 - ^3P_1) = 0.35(10)$, as estimated in Appendix B. The final result for $|\beta|$ is then

$$|\beta| = 2.18(33) \times 10^{-8} \text{ ea}_0/(\text{V/cm}). \tag{5.7}$$

This result is in good agreement with the semi-empirical estimate of Section V A as well as the calculation of Ref. [2].

The 15% uncertainty in $|\beta|$ is dominated by the uncertainty in BF_1. A measurement of BF_1 using an Yb hollow cathode lamp and a spectrometer is currently being pursued in this laboratory in order to reduce the uncertainty in $|\beta|$. Anticipating a precise measurement of the branching fraction, we also give the result in terms of $BF_1(^3D_1 - ^3P_1)$:

$$|\beta| = \frac{1.29(4) \times 10^{-8} \text{ ea}_0/(\text{V/cm})}{\sqrt{BF_1}}. \tag{5.8}$$

If the uncertainty in BF_1 can be reduced sufficiently, the relative uncertainty in $|\beta|$ will be reduced to 4%, dominated by the errors in the calibration of the photodiode sensitivities.

E. Magnetic Dipole Amplitude

By turning off the DC electric field in the apparatus and attempting to observe the 408 nm transition, we were able to put a limit on the magnetic dipole transition amplitude for the $6s^2\ ^1S_0 \rightarrow 5d6s\ ^3D_1$ transition. We compared fluorescence signals taken at 0 and 45 kV/cm. Measurements at 45 kV/cm were taken both before and after the measurement at 0 kV/cm to make sure that the frequency of the laser remained locked. At the 90% confidence level, we find that

$$|M1| < 0.015\ \mu_B. \tag{5.9}$$

A more sensitive measurement of $M1$ is currently being made in this laboratory [29]. This measurement will be sensitive to the interference of the Stark-induced and magnetic dipole transition amplitudes.

VI. ELECTRIC QUADRUPOLE MOMENT AND TENSOR POLARIZABILITY OF THE 404 NM TRANSITION

The $6s^2\ ^1S_0 \rightarrow 5d6s\ ^3D_2$ transition occurs at 404 nm. The transition rate involves both electric quadrupole and Stark-induced amplitudes. In a 15 kV/cm electric field, the two amplitudes are roughly equal. The contribution of both amplitudes to the transition rate is observed and their absolute strengths are measured by the same method as the 408 nm transition.

A. Electric Quadrupole Transition Amplitude

The electric quadrupole transition amplitude is given by [30]

$$E2 = \langle 5d6s\ ^3D_2, m| \sum_q (-1)^q\ Q^2_q (\nabla\varepsilon)^2_{-q} |6s^2\ ^1S_0, 0\rangle \tag{6.1}$$

where

$$Q^2_0 = \frac{-e}{2}(3z^2 - r^2)\ ,\ Q^2_{\pm 1} = \frac{\pm e\sqrt{3}}{\sqrt{2}} z(x \pm iy)\ ,$$
$$Q^2_{\pm 2} = \frac{-e\sqrt{3}}{2\sqrt{2}}(x \pm iy)^2$$

and

$$(\nabla\boldsymbol{\varepsilon})^2_0 = \frac{\partial \varepsilon_z}{\partial z}\ ,$$
$$(\nabla\boldsymbol{\varepsilon})^2_{\pm 1} = \pm\frac{1}{\sqrt{6}}\left(\left(\frac{\partial}{\partial x} \pm i\frac{\partial}{\partial y}\right)\varepsilon_z + \frac{\partial}{\partial z}\left(\varepsilon_x \pm i\varepsilon_y\right)\right)\ ,$$
$$(\nabla\boldsymbol{\varepsilon})^2_{\pm 2} = \frac{1}{\sqrt{6}}(\frac{\partial}{\partial x} \pm i\frac{\partial}{\partial y})(\varepsilon_x \pm i\varepsilon_y).$$

Q^2_q and $(\nabla\boldsymbol{\varepsilon})^2_q$ are operator components in a spherical basis of the electric quadrupole moment and the second rank tensor formed by the electric field gradient.

For a monochromatic plane wave traveling in the x-direction, $\boldsymbol{\varepsilon}(\mathbf{r}) = \boldsymbol{\varepsilon} e^{ikx}$ and $\varepsilon_x = 0$, so

$$(\nabla\boldsymbol{\varepsilon})^2_0 = 0\ ,\ (\nabla\boldsymbol{\varepsilon})^2_{\pm 1} = \pm\frac{i}{\sqrt{6}} k\varepsilon_z\ ,\ (\nabla\boldsymbol{\varepsilon})^2_{\pm 2} = \mp\frac{1}{\sqrt{6}} k\varepsilon_y. \tag{6.2}$$

Here, $k = 2\pi/\lambda$.

With L-S coupling, the electric quadrupole matrix element is zero between states of different S. However, the nominal $^3D_2$ state has some admixture of $^1D_2$ due to spin-orbit interaction, leading to a nonzero transition amplitude. A rough estimate of the $(^3D_2\|Q^2\|^1S_0)$ reduced electric quadrupole matrix element has been made using Hartree-Fock wavefunctions [31], giving

$$\chi \equiv \frac{1}{\sqrt{5}}(^3D_2\|Q^2\|^1S_0)$$
$$\simeq 0.5(4)\ \mathrm{ea}_0^2. \quad \text{(estimate)} \tag{6.3}$$

Introduction of χ simplifies subsequent discussion.

B. Tensor Transition Polarizability

In the presence of a static electric field, $\mathbf{E}$, and an oscillating electric field, $\boldsymbol{\varepsilon}$, the Stark-induced amplitude between the perturbed $|^1S_0, 0\rangle$ state and the perturbed $|^3D_2, m\rangle$ state is

$$E1_{St} = \langle\overline{5d6s^3D_2, m}| -\mathbf{d}\cdot\boldsymbol{\varepsilon}\,|\overline{6s^2{}^1S_0, 0}\rangle$$
$$\equiv \gamma G^2_m, \tag{6.4}$$

where

$$G^2_0 = \frac{1}{\sqrt{6}}(-\varepsilon_x E_x - \varepsilon_y E_y + 2\varepsilon_z E_z)\ ,$$
$$G^2_{\pm 1} = \pm\frac{1}{2}((\varepsilon_x \pm i\varepsilon_y)E_z + \varepsilon_z(E_x \pm iE_y))\ ,$$
$$G^2_{\pm 2} = \frac{1}{2}((\varepsilon_x \pm i\varepsilon_y)(E_x \pm iE_y)).$$

The G^2_m are the spherical components of a second rank tensor. Only the tensor transition polarizability is nonzero since the transition is $J = 0 \to J' = 2$. The single parameter γ completely determines the Stark-induced transition amplitude for any arrangement of $\mathbf{E}$ and $\boldsymbol{\varepsilon}$.

We apply a static electric field in the z-direction and the light propagates in the x-direction, so $\mathbf{E} = E_z$ and $\varepsilon_x = 0$ and the G^2_m reduce to

$$G^2_0 = \sqrt{\frac{2}{3}}\varepsilon_z E_z\ \ ,\ \ G^2_{\pm 1} = \frac{i}{2}\varepsilon_y E_z\ \ ,\ \ G^2_{\pm 2} = 0. \tag{6.5}$$

Ref. [13] uses semi-empirical estimates of the relevant dipole matrix elements to estimate the tensor transition polarizability:

$$|\gamma| \simeq 65(65)\ a_0^3$$
$$\simeq 1.3(1.3)\times 10^{-8}\ \mathrm{ea}_0/(\mathrm{V/cm}). \quad \text{(estimate)} \tag{6.6}$$

The large uncertainty is due to a cancellation of terms in the calculation.

C. Angular Distribution of Fluorescence

Measurements of E2 and tensor transition polarizability (χ and γ) were made using only even isotopes in order to avoid the added complexity of hyperfine structure. Using the density matrix formalism, we determined the relative contributions of χ and γ to the fluorescence signal due to excitation with 404 nm light. The fluorescence signal due to excitation with 556 nm light was again used to remove dependence on the atomic beam density and the fluorescence detection efficiency. A derivation using the density matrix formalism is given in Ref. [13]. The ratio of the signals due to 404 and 556 nm excitation is

$$\frac{\frac{F(404,\hat{y})}{I(404,\hat{y})}}{\frac{F(556,\hat{y})}{I(556,\hat{y})}} = \frac{BF_2}{\frac{1}{3}|(^3P_1\|r\|^1S_0)|^2}\frac{404}{556}\quad (0.333\ k^2\chi^2$$
$$+\ 0.298\ E^2\gamma^2). \tag{6.7}$$

BF_2 is the $^3D_2 \to {}^3P_1$ branching fraction.

D. Results

The ^{172}Yb component in the 404 nm transition was used for these measurements since it is the strongest isolated line. $|\chi|$ and $|\gamma|$ were measured with 404 and 556 nm light both polarized in the y-direction. $|\chi|$ was measured at zero electric field while $|\gamma|$ was determined by measuring the fluorescence with an electric field of 33 kV/cm and subtracting off the measured contribution from χ. Using $|(^3P_1\|r\|^1S_0)| \simeq 0.549(4)$ a_0 and $BF_2 = 0.88(5)$, as estimated in Ref. [13], we obtain

$$|\chi| = 0.65(3)\ \mathrm{ea}_0{}^2 \tag{6.8}$$

and

$$|\gamma| = 4.1(2) \times 10^{-8}\ \mathrm{ea_0/(V/cm)}. \quad (6.9)$$

As discussed in Ref. [13], the estimate of $BF_2(^3D_2 - {}^3P_1)$ is more robust than $BF_1(^3D_1 - {}^3P_1)$, so here the branching fraction is not the dominant source of uncertainty as it was for the measurement of $|\beta|$ for the 408 nm transition. The branching fraction uncertainty along with the uncertainty in the calibration of the photodiodes results in a 5% uncertainty in the measurements of $|\chi|$ and $|\gamma|$.

Given the large uncertainties in the estimates of χ and γ (see Eqs. 6.3 and 6.6), the apparent disagreement between the measurements and those estimates does not appear significant. As discussed in Ref. [13], the value of γ, the tensor transition polarizability, may be sensitive to configuration mixing in the $^1P_1$ state.

These measurements on the 404 nm transition are useful in evaluating the feasibility of a measurement of parity nonconservation in this transition. Such a measurement would be sensitive only to the nuclear spin-dependent term in the weak Hamiltonian. With an electric field larger than 15 kV/cm, $E^2\gamma^2$ dominates over $k^2\chi^2$. However, the presence of a sizeable electric quadrupole transition amplitude may make a Stark-PNC interference measurement problematic. In general the Stark-induced electric dipole and the electric quadrupole amplitudes can interfere. Even with an experimental geometry designed to suppress Stark-E2 interference, misalignments induce interference terms at some level, indistinguishable from the Stark-PNC interference. Any concrete proposal for a measurement of parity nonconservation on the 404 nm transition should address these problems quantitatively.

VII. SUMMARY

We have measured the DC Stark shifts, hyperfine structure, and isotope shifts for the Stark-induced $6s^2\,{}^1S_0 \rightarrow 5d6s\,{}^3D_{1,2}$ transitions. We have also made absolute measurements of the vector polarizability, $|\beta|$, for the $^3D_1$ transition as well as the $E2$ transition amplitude and the tensor transition polarizability, $|\gamma|$, for the $^3D_2$ transition.

Since several frequency components overlap in the transitions studied, it is useful to have accurate frequency shift measurements in order to plan and interpret a measurement of PNC in different isotopic and hyperfine components. The absolute measurement of the vector transition polarizability will allow $M1$ and $E1_{\mathrm{PNC}}$ to be measured absolutely by Stark interference. These measurements are also useful for testing the accuracy of calculations of atomic matrix elements.

Our experimental upper limit on the $M1$ transition amplitude shows that it is suppressed. The $E2$ amplitude for the $^3D_2$ transition is measured to be only moderately suppressed, as expected. This measurement is useful for evaluating the feasibility of observing nuclear spin-dependent PNC in this transition.

ACKNOWLEDGMENTS

The authors are grateful to E.D. Commins and D.S. Weiss for many useful discussions. This work was supported by the U.S. Department of Energy under Contract No. DE-AC03-76SF00098 and by the UC Berkeley Committee on Research. J.E.S. was a Berkeley Undergraduate Research Scholar.

APPENDIX A: CALCULATION OF ANGULAR DISTRIBUTION OF FLUORESCENCE

In order to simplify the discussion, we will only consider the even isotopes of Yb, i.e. those with zero nuclear spin. The experimental geometry is shown in Figure 5.

Generally, the angular distribution of fluorescence from $^3P_1$ depends not only on the populations of the m_J sublevels, but also on the coherence among the sublevels. We therefore use the density matrix formalism. (See for example, Ref. [32].)

We measure the relative strengths of the two transitions (404 or 408 nm versus 556 nm). Here we only discuss the case of the 408 nm transition; a similar derivation for the 404 nm transition is given in Ref. [13]. Both lasers are tuned to the line centers, interacting with atoms with near-zero transverse velocity. The laser linewidths, the natural linewidths, and transit linewidth are all much smaller than the Doppler width of the atomic beam, so the absorption profiles are flat over the relevant spectral intervals.

We first consider the fluorescence at 556 nm produced by excitation of $^3D_1$ with 408 nm light polarized linearly in y. In steady state, the density matrix of the $^3D_1$ level, in the basis where z is the axis of quantization, is

$$\rho^{^3D_1}(408,\hat{y}) = \frac{4\pi^2}{\hbar^2 c}\beta^2 E^2 I(408,\hat{y}) \times \begin{pmatrix} 1/2 & 0 & -1/2 \\ 0 & 0 & 0 \\ -1/2 & 0 & 1/2 \end{pmatrix} \rho_\omega^{^1S_0}(408)\tau(^3D_1), \quad (A1)$$

where the order of states in both the rows and columns of the density matrix is $m_J = -1$, $m_J = 0$, $m_J = +1$, $I(408,\hat{y})$ is the intensity of the light, and $\rho_\omega^{^1S_0}(408)$ is the density of the ground state per unit frequency, defined by

$$\rho_\omega = \frac{c}{\omega_0}\rho_v = \frac{\lambda_0}{2\pi}\rho_v \quad (A2)$$

where ρ_v is the density per unit velocity, and ω_0 and λ_0 are the resonance frequency and wavelength.

Eq.A1 shows that since the Stark-induced amplitude is proportional to $\boldsymbol{\varepsilon}\times\mathbf{E}$, for $\boldsymbol{\varepsilon} = |\varepsilon|\hat{y}$ and $\mathbf{E} = |\mathbf{E}|\hat{\mathbf{z}}$, we get an excited state aligned in x.

In the presence of external electric and magnetic fields, the m_J sublevels are no longer degenerate, so the off-diagonal elements of the density matrix average out due

to oscillations, with a frequency determined by the energy difference between the associated sublevels. A 1.3 Gauss magnetic field in the z-direction assures that the splitting between the m_J=+1 and m_J=-1 sublevels produces oscillations in the off-diagonal density matrix elements of the $^3D_1$ and $^3P_1$ levels at frequencies higher than the relaxation rates of the two levels due to spontaneous emission. Therefore, we make the simplifying approximation that

$$\rho_{1,-1} = \rho_{-1,1} = 0 \tag{A3}$$

when calculating observables that depend on spontaneous emission from these levels. In Ref. [13] the validity of this approximation was investigated in detail by calculating and measuring the fluorescence dependence on the applied magnetic field. It was shown that the error introduced by this approximation is negligible.

The approximation of Eq.A3 allows us to replace Eq. A1 with

$$\rho^{^3D_1}(408,\hat{y}) = \frac{4\pi^2}{\hbar^2 c}\beta^2 E^2 I(408,\hat{y}) \times \begin{pmatrix} 1/2 & 0 & 0 \\ 0 & 0 & 0 \\ 0 & 0 & 1/2 \end{pmatrix} \rho_\omega^{^1S_0}(408)\tau(^3D_1). \tag{A4}$$

Considering the decay $^3D_1 \rightarrow ^3P_1$ then results in a steady state density matrix for $^3P_1$ of

$$\rho^{^3P_1}(408,\hat{y}) = \frac{4\pi^2}{\hbar^2 c}\beta^2 E^2 I(408,\hat{y}) BF_1 \times \begin{pmatrix} 1/4 & 0 & 0 \\ 0 & 1/2 & 0 \\ 0 & 0 & 1/4 \end{pmatrix} \rho_\omega^{^1S_0}(408)\tau(^3P_1), \tag{A5}$$

where BF_1 is the $^3D_1 \rightarrow ^3P_1$ branching fraction.

We observe fluorescence predominantly in a cone of $\approx 25^\circ$ half angle around the z-axis. However, the detailed angular dependence of the fluorescence detection efficiency is very complicated. It depends on the position of the laser beams relative to the holes in the top electrode, the reflectivity of the bottom electrode, the detailed behavior of light in the Lucite light guide, and the angular dependence of the interference filter transmission and phototube responsivity. In order to eliminate uncertainties associated with estimating these factors, we create the same distribution of density matrix elements in $^3P_1$ by exciting with 556 nm light. In the steady state, 556 nm light linearly polarized in the y-direction generates

$$\rho^{^3P_1}(556,\hat{y}) = \frac{4\pi^2}{\hbar^2 c}\frac{1}{3}e^2|(^3P_1\|r\|^1S_0)|^2 I(556,\hat{y}) \times \begin{pmatrix} 1/2 & 0 & 1/2 \\ 0 & 0 & 0 \\ 1/2 & 0 & 1/2 \end{pmatrix} \rho_\omega^{^1S_0}(556)\tau(^3P_1), \tag{A6}$$

which becomes

$$\rho^{^3P_1}(556,\hat{y}) = \frac{4\pi^2}{\hbar^2 c}\frac{1}{3}e^2|(^3P_1\|r\|^1S_0)|^2 I(556,\hat{y}) \times \begin{pmatrix} 1/2 & 0 & 0 \\ 0 & 0 & 0 \\ 0 & 0 & 1/2 \end{pmatrix} \rho_\omega^{^1S_0}(556)\tau(^3P_1) \tag{A7}$$

after setting the off-diagonal elements to zero (Eq. A3). 556 nm light polarized in z generates

$$\rho^{^3P_1}(556,\hat{z}) = \frac{4\pi^2}{\hbar^2 c}\frac{1}{3}e^2|(^3P_1\|r\|^1S_0)|^2 I(556,\hat{y}) \times \begin{pmatrix} 0 & 0 & 0 \\ 0 & 1 & 0 \\ 0 & 0 & 0 \end{pmatrix} \rho_\omega^{^1S_0}(556)\tau(^3P_1). \tag{A8}$$

By taking the average of the fluorescence signals obtained with the 556 nm excitation light polarized in y and z and comparing with the fluorescence signal obtained with 408 nm excitation light polarized in y, we eliminate any effect of the angular dependence of the fluorescence detection efficiency. Any particular fluorescence detection geometry can be represented by a fluorescent light monitoring operator L_F. The observed fluorescence signal, F, is then given by [32]

$$F = \mathrm{Tr}(\rho L_F). \tag{A9}$$

where ρ represents the excited state density matrix. The fluorescence signal at 556 nm produced by 408 nm light polarized in y is then given by

$$\begin{aligned} F(408,\hat{y}) &= \mathrm{Tr}\left(\rho^{^3P_1}(408,\hat{y})L_F\right) \\ &= \frac{4\pi^2}{\hbar^2 c}\beta^2 E^2 I(408,\hat{y}) BF_1 \rho_\omega^{^1S_0}(408) \\ &\quad \times \mathrm{Tr}\left(\begin{pmatrix} 1/4 & 0 & 0 \\ 0 & 1/2 & 0 \\ 0 & 0 & 1/4 \end{pmatrix} L_F\right). \end{aligned} \tag{A10}$$

The fluorescence signals at 556 nm produced by 556 nm light polarized in y and z respectively, are given by

$$F(556,\hat{y}) = \frac{4\pi^2}{\hbar^2 c}\frac{1}{3}e^2|(^3P_1\|r\|^1S_0)|^2 I(556,\hat{y})\rho_\omega^{^1S_0}(556) \times \mathrm{Tr}\left(\begin{pmatrix} 1/2 & 0 & 0 \\ 0 & 0 & 0 \\ 0 & 0 & 1/2 \end{pmatrix} L_F\right), \tag{A11}$$

$$F(556,\hat{z}) = \frac{4\pi^2}{\hbar^2 c}\frac{1}{3}e^2|(^3P_1\|r\|^1S_0)|^2 I(556,\hat{z})\rho_\omega^{^1S_0}(556) \times \mathrm{Tr}\left(\begin{pmatrix} 0 & 0 & 0 \\ 0 & 1 & 0 \\ 0 & 0 & 0 \end{pmatrix} L_F\right). \tag{A12}$$

By forming the ratio R_F we eliminate the dependence on L_F:

$$R_F \equiv \frac{\frac{F(408,\hat{y})}{I(408,\hat{y})}}{\frac{1}{2}\left(\frac{F(556,\hat{y})}{I(556,\hat{y})}+\frac{F(556,\hat{z})}{I(556,\hat{z})}\right)} = \frac{\beta^2 E^2 BF_1 \rho_\omega^{^1S_0}(408)}{\frac{1}{3}e^2|(^3P_1\|r\|^1S_0)|^2\rho_\omega^{^1S_0}(556)} = \frac{\beta^2 E^2 BF_1}{\frac{1}{3}e^2|(^3P_1\|r\|^1S_0)|^2}\times\frac{408.3}{555.8}. \quad \text{(A13)}$$

Using the measured angular acceptance of the interference filter and geometrical considerations, we have estimated the fluorescence signal after 556 nm excitation with z-polarization to be ≈0.07 of that with y-polarization. A direct measurement of the ratio gives a somewhat higher value

$$\frac{\frac{F(556,\hat{z})}{I(556,\hat{z})}}{\frac{F(556,\hat{y})}{I(556,\hat{y})}} = 0.15(1). \quad \text{(A14)}$$

This value remained constant over the course of the measurements of β.

Taking the average of the measured values for the two polarizations eliminates the need to rely on uncertain estimates of the angular dependence of the fluorescence detection. Using the direct measurement from Eq. A14, we find that

$$R_F = \frac{\frac{F(408,\hat{y})}{I(408,\hat{y})}}{\frac{1.15}{2}\frac{F(556,\hat{y})}{I(556,\hat{y})}} = \frac{\beta^2 E^2 BF_1}{\frac{1}{3}e^2|(^3P_1\|r\|^1S_0)|^2}\times\frac{408.3}{555.8}. \quad \text{(A15)}$$

Since the density of the atomic beam changes very little over the dimensions of the laser beams and the transition is not being saturated, we can measure the intensity of the light integrated over the laser beam cross-section. We can therefore interpret I in these equations as the total power in each laser beam.

APPENDIX B: THE $^3D_1$ - $^3P_1$ BRANCHING FRACTION

Assuming pure configurations and pure L-S coupling for $^3D_1$ and $^3P_{0,1,2}$, the branching fractions are found to be 0.64, 0.35, and 0.01, respectively. $^3D_1$ appears to be well described by a single configuration and L-S state [24]. However, this is not true for the ^3P states. Spin-orbit mixing has negligible effect, but it is difficult to account for the presence of the 5d6p configuration in addition to the dominant 6s6p configuration in $^3P_{0,1,2}$. The multi-configuration Dirac-Fock calculations of Ref. [24] give values of 0.13-0.16 for the amplitude of the 5d6p configuration in $^3P_{0,1,2}$. The 5d6p contribution to each decay amplitude could then interfere with the dominant 6s6p contribution, changing the decay rates by up to 30%. The effect of changes in decay rates on the branching fractions depends on relative signs and magnitude of the amplitudes.

A direct measurement of the intensities of the three transitions of interest has been made using an electrodeless discharge tube and a Fourier transform spectrometer [33,25]. However, there are significant uncertainties in extracting the branching fraction from this measurement [34]. One can use the stated intensity values for the three transitions to derive the values 0.5, 0.4, and 0.2 for the $^3P_{0,1,2}$ branching fractions. Within the large uncertainties, these measurements are in reasonable agreement with the estimate above.

It should be possible to measure this branching fraction to a few percent with either a Fourier transform spectrometer or a grating spectrometer with a hollow cathode lamp as a source [35,36]. The use of Ar buffer gas in the hollow cathode lamp provides reference lines which can be used to calibrate the relative detection efficiency of the spectrometer *in situ* [37]. A measurement of this branching fraction is currently being made in this laboratory.

For the present work, we adopt the value BF_1=0.35(10) for the $^3D_1$ - $^3P_1$ branching fraction obtained assuming pure configurations and L-S coupled states. The uncertainty reflects possible effects of other configurations on this estimate.

---

† Present address: SBC Technology Resources Inc., 9505 Arboretum Blvd., Austin, TX 78759.

* Present address: Max Planck Institute for Nuclear Physics, 69029 Heidelberg, Germany.

[1] D. DeMille, Phys. Rev. Lett. **74**, 4165 (1995).

[2] S.G. Porsev, Yu.G. Rakhlina, and M.G. Kozlov, Pis'ma Zh. Eksp. Teor. Fiz. **61**, 449 (1995) [JETP Lett. **61** 459 (1995)].

[3] B.P. Das, Phys. Rev. A **56**, 1635 (1997).

[4] M.A. Bouchiat and C. Bouchiat, Rep. Prog. Phys. **60**, 1351 (1997).

[5] D. Budker, WEIN 1998 Proceedings.

[6] C.Wieman, ICAP 1998 Proceedings.

[7] M.A. Bouchiat, *et al.* , Phys. Lett. B **117B**, 358 (1982); Phys. Lett. B **134B**, 463 (1984); J. Phys. **47**, 1709 (1986);

[8] S.L. Gilbert, R.N. Watts and C.E. Wieman, Phys. Rev. A **29**, 137 (1983); M.S. Noecker, B.P. Masterson, and C.E. Wieman, Phys. Rev. Lett. **61**, 310 (1988).

[9] P. Drell and E.D. Commins, Phys. Rev. Lett. **53**, 968 (1984); Phys. Rev. A **32**, 2196 (1985).

[10] C.S. Wood, *et al.* , Science **275**, 1759 (1997).

[11] V.A. Dzuba, V.V. Flambaum, and I.B. Khriplovich, Z. Phys. D **1**, 243 (1986).

[12] D. Weiss, Ph. D. thesis, Stanford University(1993).

[13] C.J. Bowers, Ph. D. thesis, University of California at Berkeley (1993). (http://phylabs.berkeley.edu/bowers-/dl_thesis.html)

[14] R.W.P. Drever, *et al.* Appl. Phys. B **31**, 97 (1983).

[15] W. Baumann and R. Mecke, Z. Phys. **81**, 445 (1933).

[16] D. Wandt, *et al.* Opt. Comm. **130**, 81 (1996).
[17] N.P. Buslenko *et al.* *The Monte Carlo method; the method of statistical trials*, edited by Yu. A. Shreider (Pergamon Press, Oxford, 1966).
[18] J.R.P. Angel and P. G. H. Sandars, Proc. Roy. Soc. A **305**, 125 (1968).
[19] O. Töpper, G.H. Guthöhrlein, and P. Hillerman, European Group for Atomic Spectroscopy (1997), conference abstracts.
[20] S.G. Porsev, Y.G. Rakhlina, and M.G. Kozlov, to appear in J.Phys.B.
[21] W.H. King, *Isotope Shifts in Atomic Spectra*, (Plenum Press, New York, 1984).
[22] W.H. King, J. Opt. Soc. Am. **53**, 638 (1963).
[23] D.L. Clark, *et al.* Phys. Rev. A **20**, 239 (1979).
[24] J. Migdalek and W.E. Baylis, At. Mol. Opt. Phys. **24**, L99 (1991).
[25] J.-F. Wyart and P. Camus, Phys. Scr. **20**, 43 (1979).
[26] M.A. Bouchiat and C. Bouchiat, J. Phys. **36**, 493 (1975).
[27] D. Brown and D. Budker (to be published).
[28] D. DeMille, D. Budker, and E.D. Commins, Phys. Rev. A **50** (6), 4657 (1994).
[29] J. Stalnaker, Undergraduate thesis, University of California at Berkeley (1998).
[30] N.F. Ramsey, *Molecular Beams*, (Oxford University Press, Oxford, 1956).
[31] V.A Dzuba (dzuba@ugrad.phys.unsw.edu.au), (private communication).
[32] A. Corney, *Atomic and Laser Spectroscopy*, (Oxford University Press, Oxford, 1977).
[33] J. Vergès, Unpublished (1978).
[34] J. Vergès (verges@lx5.lac.u-psuf.fr), private communication.
[35] G. Nave (gnave@nist.gov), private communication.
[36] J. Lawler (jelawler@facstaff.wisc.edu), private communication.
[37] W. Whaling, *et al.* J. Quant. Spectrosc. Radiat. Transfer **50**, 7 (1993).

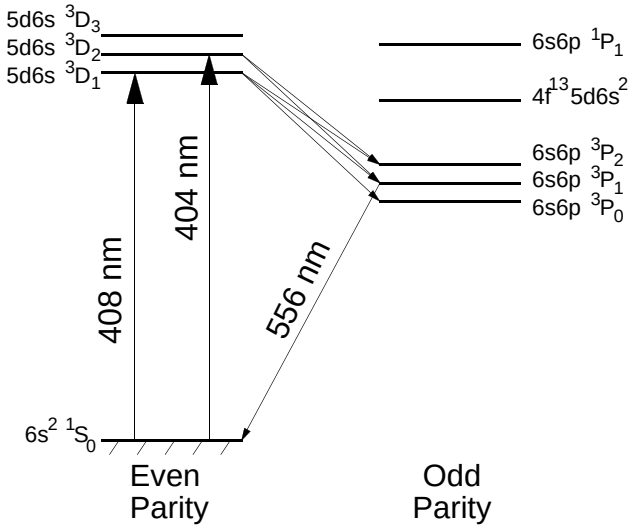

FIG. 1. Low-lying energy levels of atomic Yb.

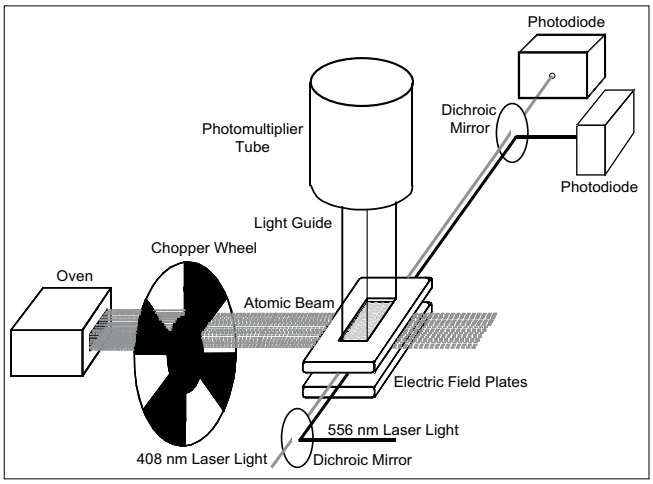

FIG. 2. Schematic of apparatus.

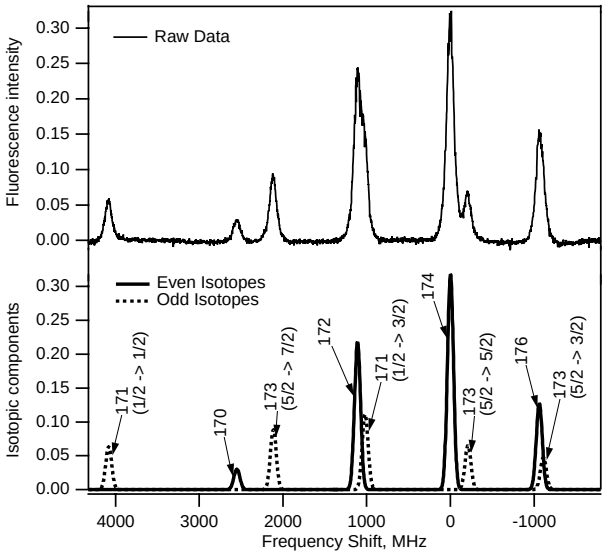

FIG. 3. Laser-excitation spectrum of the 408 nm transition observed via fluorescence at 556 nm, and contributions from individual lines as expected from natural isotopic abundances and extracted values of the hyperfine splittings and isotope shifts.

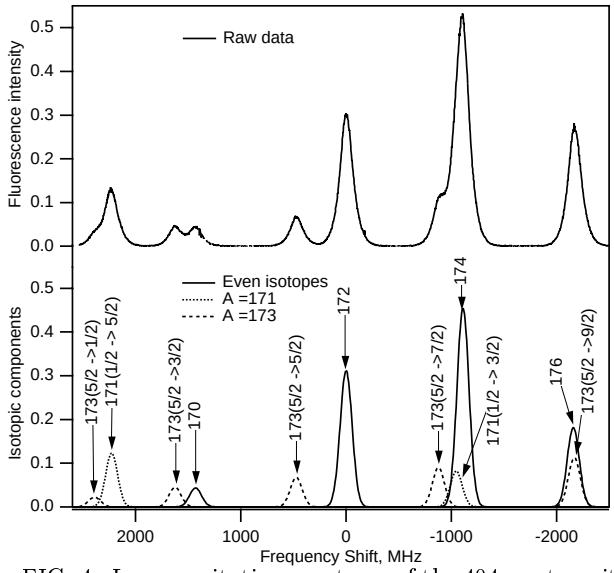

FIG. 4. Laser-excitation spectrum of the 404 nm transition observed via fluorescence at 556 nm, and contributions from individual lines as expected from natural isotopic abundances and extracted values of the hyperfine splittings and isotope shifts.

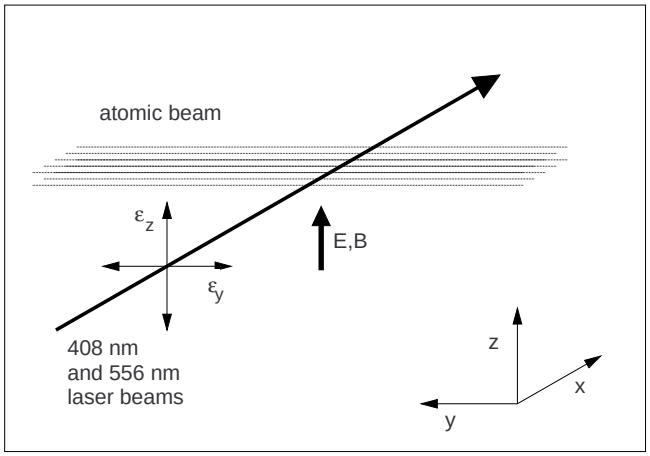

FIG. 5. Experimental geometry for measurement of $|\beta|$.

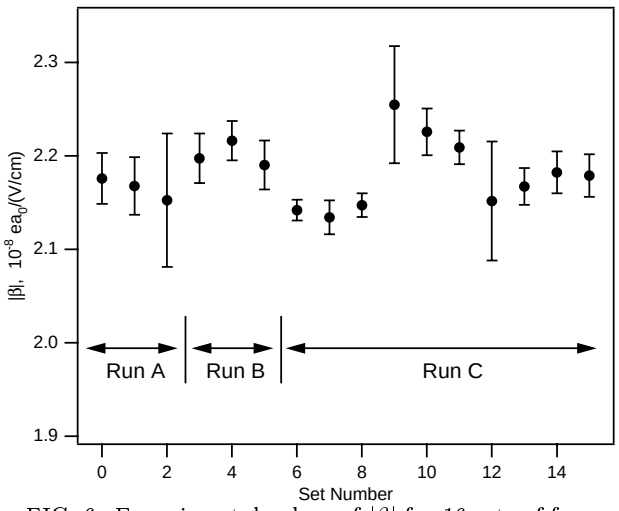

FIG. 6. Experimental values of $|\beta|$ for 16 sets of frequency scans.

TABLE I. Frequency shifts for the 408 nm transition measured at 45 kV/cm.

Isotope	Hyperfine Component	Shift(MHz)
171	$F=1/2 \rightarrow F'=1/2$	4082(2)
170		2551(2)
173	$F=5/2 \rightarrow F'=7/2$	2115(2)
172		1110(2)
171	$F=1/2 \rightarrow F'=3/2$	1019(2)
174		0
173	$F=5/2 \rightarrow F'=5/2$	-209(2)
176		-1061(2)
173	$F=5/2 \rightarrow F'=3/2$	-1110(2)

TABLE II. Shift of the center of gravity (relative to ^{174}Yb) and hyperfine constants of odd isotopes for the 408 nm transition.

	Present work			Reference. [19]	
Isotope	c.g.(MHz)	A(MHz)	B(MHz)	A(MHz)	B(MHz)
171	2035(2)	-2040(2)		-2037(9)	
173	617(2)	562.8(0.5)	337(2)	563(1)	335(1)

TABLE III. Frequency shifts for the $6s^2\,{}^1S_0 \rightarrow 5d6s\,{}^3D_2$ transition measured at 33 kV/cm with 404 nm light polarized parallel to the electric field direction.

Isotope	Hyperfine Component	Shift(MHz)
173	$F=5/2 \rightarrow F'=1/2$	2390(2)
171	$F=1/2 \rightarrow F'=5/2$	2234(2)
173	$F=5/2 \rightarrow F'=3/2$	1625(2)
170		1431(2)
173	$F=5/2 \rightarrow F'=5/2$	474(2)
172		0
173	$F=5/2 \rightarrow F'=7/2$	-887(8)
174		-1111(4)
171	$F=1/2 \rightarrow F'=3/2$	-1054(10)
176		-2159(10)
173	$F=5/2 \rightarrow F'=9/2$	-2189(10)

TABLE IV. Shift of center of gravity (relative to ^{172}Yb) and the magnetic dipole (A) and electric quadrupole (B) coefficients of odd isotopes for the 404 nm transition.

	Present work			Reference. [19]	
Isotope	c.g.(MHz)	A(MHz)	B(MHz)	A(MHz)	B(MHz)
171	919(4)	1315(4)		1311(6)	
173	-491(4)	-363.4(10)	487(5)	-362(2)	482(25)